Biofilms on glacial surfaces: hotspots for biological activity

H. J. Smith[1,2], A. Schmidt[1,3], R. Foster[4], S. Littmann[5], M. M. M. Kuypers[5], and C. Foreman[1,3]**

Supporting Information:

Supplementary Information Content:

Supplementary Materials and Methods

Supplementary Results

Supplementary References

Supplementary Figures (S1-S3)

Supplementary Tables (S1-S3)

Supplementary Materials and Methods:

Study Site and Sample Collection and Preparation

The cryoconite hole used in this study was collected during the 2011 Austral summer from the surface of the Canada Glacier (77°37' S, 162°57' E) as part of a larger sampling campaign (n=32) [1]. The ice lidded cryoconite hole was 38 cm by 34 cm with a maximum depth of 25 cm. The water depth of the sampled cryoconite hole was 12 cm and the depth of sediment was 0.5 cm. Liquid water and sediment were extracted from the glacial surface using syringes and ethanol cleaned spatulas and placed into sterile Whirl-Pak® bags. All samples were stored for three weeks at -20°C prior to further processing. Sediments (117.14 g of sediment in total) were prepared for different analytical methods in two ways; (i) 2 g were placed into sterile cryo vials and stored at -80°C for confocal laser scanning microscopy (CLSM), and (ii) 40 g were added to 500 ml of DI water and placed on an orbital shaker at 1,500 rpm at 10°C for 24 hrs as required for single cell secondary ion mass spectrometry (nanoSIMS) analyses. After shaking, the supernatant containing the dislodged bacterial cells were separated from the sediment and immediately used for subsequent analyses (see below nanoSIMS preparation section). Cryoconite from the Canada Glacier have been studied over the last several years and there is information available regarding cryoconite distribution, biogeochemical data, community structure, and exposure intervals to atmospheric conditions for cryoconites from this location [2-7]. Relevant for this study is the previously published distribution of cryoconite holes across the Canada Glacier [2] as well as rates of primary production and isolation age [1].Therefore, a single sample from the well-studied glacial surface was advantageous for the methodologically intensive nature of this study.

55

Bacterial Community Composition

Genomic DNA was extracted from 0.25 g of cryoconite sediment using a MO BIO

PowerSoil™ DNA Isolation Kit, following the manufacturer's protocol (MO BIO

Laboratories Inc., Carlsbad, CA, USA). The extracted DNA was cleaned and

concentrated with the Wizard® SV Gel and PCR Clean-Up System (Promega Corporation,

Madison, WI, USA) following established manufacturers' protocols. Small subunit rRNA

gene sequences were amplified with barcoded universal bacterial primers FD1 (5′-

ctcgcgtgtcAGAGTTTGATCCTGGCT- CAG-3′) and 529R (5′-

ctcgcgtgtcCGCGGCTGCTGGCAC- 3′) spanning the V1, V2 and V3 regions. The

amplification protocol began with a hot start (94°C for 4 min), followed by 28 cycles of a

30 s 94°C denaturation, a 1 min annealing step at 58°C, and an elongation step at 72°C

for 1 min. After the completion of the 28 amplification cycles, there was a final

elongation at 72°C for 10 min. PCR products were excised from a 0.8 % agarose gel and

cleaned using an Ultrafree®-DA gel extraction column (Millipore Corporation, Bedford,

MA, USA). The gel extract was cleaned and concentrated after the gel extraction using

the Wizard® SC Gel and PCR Clean-Up System and the dsDNA PCR product was

quantified with a Qubit fluorometer (Invitrogen, Carlsbad, CA, USA). Adaptor sequences

were ligated onto the amplicon products and sequencing was performed using a 454 GS

Jr. (454 Life Sciences, Branford, CT, USA). Sequences were trimmed to one standard

deviation below the mean sequence length, and the data was processed using the

Quantitative Insights Into Microbial Ecology (QIIME) toolkit [8]. Briefly, sequences were

clustered into OTUs using a 97% identity threshold, and the most abundant sequence

78 from each OTU was selected as a representative sequence for the OTU. Taxonomy was

79 assigned for each representative sequence using the Basic Local Alignment Search Tool

80 (BLAST) against the Silva database. Chimeric sequences were removed with Chimera

81 Slayer [9] and chimeric sequences were confirmed using Bellerophon [10]. Sequence data

82 were deposited in the NCBI SRA database under the accession number SRP073064.

83

84 **NanoSIMS Sample preparation**

85 As surface charging strongly influences secondary ion formation on particle surfaces,

86 incubations of cryoconite microbes were conducted using the detached cells in the

87 supernatant. Samples were incubated with ^{15}N-labeled ammonium chloride (~99% ^{15}N,

88 Cambridge Isotopes Laboratories Inc., Andover, MA, USA, 0.1mM final concentration)

89 and ^{13}C-labeled sodium bicarbonate (~99% ^{13}C, Cambridge Isotopes Laboratories Inc.,

90 Andover, MA, USA, 1mM final concentration) in 1 L bottles in a light incubator to

91 simulate *in situ* light (50.6 photons per m^2) and temperature (4°C) conditions for 72 hrs.

92 After incubation samples were fixed with paraformaldehyde (final concentration 2%) for

93 1.5 hrs at room temperature. Subsamples (10 ml) were then filtered onto gold-palladium

94 coated 0.2 μm GTTP polycarbonate filters (Millipore) under low vacuum pressure (< 7

95 psi) and washed three times with 1X phosphate buffered saline (PBS). Filters were dried

96 and stored in cryovials at -20°C until further processing.

97

98 **Hybridization and microscopic evaluation**

99 Sections (5 mm diameter) of the gold-paladium coated filters containing cells were

100 excised and hybridized with Fluorescent *In Situ* Hybridization (FISH) with horseradish

101 peroxidase (HRP)-labeled oligonucleotide probes following the Halogen *In Situ*

102 Hybridization Seconday Ion Mass Spectrometry (HISH-SIMS) protocol described by [11].

103 To avoid detachment of cells through sample preparation protocols the 5 mm spheres

104 were initially embedded in 0.1% low melting point agarose. For the analysis of gram–

105 negative *Bacteroidetes* bacteria, cells were permeabilized with a lysozyme (10 mg ml^{-1} in

106 0.05 M EDTA (pH 8.0) and 0.1M Tris-HCl) treatment at 37°C for 1 hr. After

107 permeabilzation filters were washed three times with ultrapure water (MQ, Millipore) and

108 endogenous peroxidases were bleached with 3% H_2O_2 for 10 min at room temperature.

109 Prior to hybridization filters were washed three times for 1 min with ultrapure water and

110 submerged in 96% ethanol for 1 min and allowed to air dry completely. Filters were

111 subjected to a 1 hr pre-hybridization step without the probe, then probes were added

112 (1:150 v/v) and hybridized at 46°C for 6 hrs using a previously described protocol[11]. The

113 following oligonucleotide probes were used to probe *Bacteroidetes* lineages: CF319a

114 (Probe Sequence (5'-3'): TGG TCC GTG TCT CAG TAC, 16S target position: 319-336,

115 formamide concentration: 35%) and CF319b (Probe Sequence (5'-3'): TGG TCC GTA

116 TCT CAG TAC, 16S target position: 319-336, formamide concentration: 35%) [12].

117 Hybridized cells were counterstained with 4',6'-diamindino-2-phenylindole (DAPI) at a

118 final concentration of 1 μg mL^{-1} in the dark for 10 min. The 5 mm filter sections were

119 covered in mountant (4 parts Citifluor (Citifluor , Ltd., London, United Kingdom), 1 part

120 VectaShield (Vector Laboratoires, Burlingame, CA)) and 10 randomly chosen fields (grid

121 size of 15625 μm^2) corresponding to 1,000-1,200 DAPI stained cells were counted using

122 a Zeiss Axioskop II fluorescence microscope (Zeiss, Berlin, Germany) with a final

123   magnification of 1,000X. Counts are reported as mean averages from triplicate cell

124   counts of cells g^{-1} of sediment that have been converted based on phylogenetic

125   classification to percentages of the total number of cells counted. *Bacteroidetes* sp. cells

126   identified with FISH and *Oscillatoria* sp. cells of interest were identified by morphology

127   and excitation under blue (450-490 nm) and green (510-560 nm) excitation filter sets and

128   imaged. Areas of interest for nanoSIMS were marked using a Laser Micro Dissection

129   (LMD) microscope 6500 (Leica, Wetzlar, Germany). Microscopic pictures were taken

130   and used for orientation purposes during the subsequent nanoSIMS analysis and for post

131   processing using look@nanoSIMS software (see below).

132   **NanoSIMS analysis**

133   NanoSIMS analysis was performed using a Cameca NanoSIMS 50 L instrument

134   (Cameca, Gennevilliers, France) at the Max Planck Institute for Marine Microbiology in

135   Bremen. After re-identifying the area of interest marked by the LMD with the nanoSIMS

136   CCD camera, samples were pre-sputtered with a Cesium (Cs^+) primary ion beam with a

137   current of ~300 pA. For the measurements a primary ion beam with a beam current

138   between 1 and 3 pA and a beam size <100 nm was used to raster the analyzed area. The

139   measurements were performed with an image size of 256 x 256 pixels over a chosen

140   raster size of 20 x 20 μm with a dwelling time of 1 or 2 ms per pixel. Mass resolving

141   power in the majority of the measurements was >8000. Negative secondary ion images of

142    $^{12}C^-$, $^{13}C^-$, $^{19}F^-$, $^{12}C^{14}N^-$, $^{12}C^{15}N^-$ and $^{32}S^-$ were recorded simultaneously with the multi-

143   collection system of the instrument. All scans (40-50 planes) were corrected for drift of

144   the beam and sample stage after acquisition and accumulated using the

145   "Look@NanoSIMS" software package (Polercky et al. 2012). Region of interest (ROIs)

146 were defined using the $^{19}F^-$ images representing the HISH labeled *Bacteroidetes* sp. cells,

147 and ROIs for the non-labeled filamentous cyanobacterial cells were chosen based on the

148 $^{12}C^{14}N$ image compared to fluorescent images for DAPI stained cells.

149   The equations used for ^{13}C and ^{15}N assimilation were as previously described in[13].

150 The cell diameter for both cyanobacterial cells and *Bacteroidetes* sp. were estimated from

151 nanoSIMS images after cells were circled using the Look@NanoSIMS software analysis

152 package [14]. Cell heights for both cell types were determined using a Nanoscope III

153 extended-multimode atomic force microscope (Vecco, Santa Barbara, CA).

154 Underestimations of cell diameter are possible due to the fixation step (2% PFA for 1.5

155 hrs). The cell diameter measures were used in equations for bio-volume estimation as

156 described in Sun and Lui (2003)[15] For filamentous cyanobacterial cells, the bio volume

157 was estimated using the equation of a cylinder:

158 $$V = (\pi/4) \; x \; d^2 \; x \; h)\qquad\qquad(1)$$

159 where d is cell diameter and h is cell height. Average height for individual cyanobacterial

160 filaments was equal to 1.57 μm.

161   For estimating bio volume of individual *Bacteroidetes* sp. cells the equation of a

162 sphere was used

163 $$(V = (\pi/6) \; x \; d^3)\qquad\qquad(2)$$

164   where d is cell diameter. The initial cellular carbon content was estimated based

165 on the relationship between bio volume and carbon content previously described in

166 Verity at al. (1992) [16]:

167 $$\text{Log}[C] = -0.363 + (0.863 \text{ x } (\text{Log}(V))) \tag{3}$$

168 Logarithms (LOG) are base 10 and C content was used to estimate the N content. As

169 none of the analyzed organisms are isolated, standard elemental analysis was not possible

170 and therefore we based our estimates of initial C and N content on the Redfield ratio

171 (C:N) of 6.6.

172   Cell specific C (A_C) and N (A_N) assimilation was calculated following the

173 equations presented in Foster et al. (2013) and are as follows:

174 $$A_C = (^{13}C_{ex} \text{ x } C_{inital})/C_{SR} \tag{4}$$

175 $$A_N = (^{15}N_{ex} \text{ x } N_{inital})/N_{SR} \tag{5}$$

176   where $^{13}C_{ex}$ and $^{15}N_{ex}$ is the atom (AT) % of ^{13}C and ^{15}N, respectively, corrected

177 for by the mean value of the respective ratios in non-enriched bulk samples (time 0)

178 measured by elemental analysis isotope ratio mass spectrometry (EA-IRMS) analyses.

179 The $C_{initial}$ and $N_{initial}$ variables are the initial C and N content as presented in equation 3,

180 while C_{SR} and N_{SR} are the labeling percentage of ^{13}C and ^{15}N, respectively, in the

181 experiment. The calculated assimilation values were divided by the incubation time (h) to

182 determine the cell specific C fixation and N fixation rates. It should be noted that there is

183 the potential for a dilution of ^{13}C and ^{15}N signals as a result of the HISH-SIMS fixation

184 procedures, and hence the calculated uptake rates potentially underestimate rates of

185 incorporation [17].

186   It was recently highlighted that microbial cells interact at the microscale [18], to

187 investigate these microscale interactions and to quantify the C and N transfer from

188   autotrophic *Oscillatoria* sp. to heterotrophic *Bacteroidetes* sp., the enrichment (AT% 13C

189   and AT% 15N) measured in the *Bacteroidetes* cells was divided into two groups and

190   include values from cell residing: close (< 2 μm) or far (> 2 μm) from a *Oscillatoria* sp.

191   cell. Phytoplankton exudates are known to form diffusion limited chemical gradients

192   around the cell surface, [19,20] the diffusivity of this boundary layer can be estimated using

193   the relationship between cell size and organic matter leakage calculated according to

194   Jackson (1987) [20]. Where ϕ is the relationship between the cell radius and cell carbon

195   content, as determined by Mullin et al. (1966) [21] for planktonic photoautotrophic

196   organisms:

197

198 $$\phi = ba^{2.28} \tag{1}$$

199

200   Where b is a constant equal to 2.67 x 10^{-4} mol multiplied by the cells radius a = 1.99

201   μm$^{2.28}$. Organic matter leakage was subsequently calculated according to Jackson (1987)

202   [20]:

203

204 $$C = \left(\frac{L}{4\pi D}\right) r^{-1} + C_{\infty} \tag{2}$$

205

206   Where the carbon leakage rate of $L = f\mu\phi$. Standard values from Jackson (1987) were

207   used for the following parameters: where f is the organic matter leakage rate from

208   photoautotrophic cells, μ is the specific growth rate, D is the molecular diffusivity of

209   organic matter, r^{-1} is the distance from the cell surface. C_{∞}, the concentration in the bulk

210   which was assumed to be nominally small and therefore set to zero. The concentration of

211 exuded organic matter was then calculated incrementally for distances ranging from very

212 near the cell surface (0.1 μm) to 10 μm away from the cell surface. To preserve these

213 distances and inhibit cell loss or movement through sample preparation and analysis

214 filters were covered with a thin layer of low met agarose (0.1%) after the initial sample

215 filtration. Using the *stats* package in R [22] a two-way ANOVA with section and distance

216 as factors was used to separately analyze ^{13}C and ^{15}N AT% enrichment of both the close

217 and far *Bacteroidetes* sp. cells. The model included either ^{13}C AT% or ^{15}N AT% as a

218 response to an interaction effect added for each analyzed section and distance from

219 filament.

220

221 **CLSM imaging and data processing**

222 For imaging, cryoconite particles were thawed on ice, placed into a sterile petri dish and

223 stained for 20 min in the dark. Fully hydrated cryoconite particles were stained with

224 either SYBR Green, a nucleic acid stain (Invitrogen; Life Technologies) 40X final

225 concentration; or calcofluor white, which is typically used for staining of chitin, cellulose

226 and polysaccharides [23] (Fluka; Sigma-Aldrich) final concentration 1 μM. After staining,

227 cryoconite particles were rinsed with 0.2 μm filter sterilized DI water three times to

228 remove any excess stain. Stains were chosen for this study after comparing a variety of

229 different stains to determine which stains would be the most sample appropriate and the

230 least reactive with abiotic material. Sediment samples were imaged with a Leica TCS

231 SP5 II upright confocal microscope using either a 25X water immersion objective, 0.95

232 NA, WD 2.5 mm; or a 63X water immersion objective, 0.9 NA, WD 2.2 mm.

233 Fluorophore excitation lasers and emission bandwidths are as follows:

234   SYBR Green (ex 497/em 520) 488 nm excitation, 500–550 nm emission collection;

235   autofluorescence, 561 nm excitation, 580–700 nm emission collection; calcofluor white

236   (ex 355, em 433), 405 nm excitation, 450–490 nm emission collection; and reflection

237   imaging, 488 nm excitation. A minimum of 10 randomly selected images were collected

238   to enumerate cellular biomass (SYBR green, autofluoresence, reflection) and biotic

239   material biomass (calcofluor white and reflection). Z-stacks were collected in either 0.54

240   μm steps for the 25X objective or 0.64 μm steps for the 63X objective. To ensure that the

241   stains selected for this study were not binding to abiotic material cryoconite particles

242   were combusted at 450°C for 5 hrs to remove any biotic material present. Combusted

243   particles were then stained and imaged following the same protocol as previously

244   described. The 3D structure of individual cryoconite particles and associated biotic

245   material was reconstructed from the CLSM images using IMARIS software (version

246   7.6.4). Surface area (μm^2) for each channel imaged was determined using the surface area

247   calculation function in the IMARIS software. Surface area calculation parameters were

248   optimized to sample and image specific properties. For the autofluorescent and SYBR

249   Green images used to quantify individual cells images were smoothed at a surface area

250   detail level of 0.5 μm^2, thresholding was based on a background subtraction method, and

251   all voxels greater than zero were collected. Biofilm images were processed with the same

252   parameters described above, with the exception that all voxels greater than 10 were

253   collected. Sediment surface area was calculated the same way as for biofilm except that

254   the surface was divided in half based on the inability of light to penetrate the sediment

255   samples and the resulting overestimation of surface area. Calculated surface areas for

256   cells identified with SYBR Green or autofluoresence, and biotic material were all

257 normalized to the surface area of cryoconite particles in the corresponding field of view

258 analyzed.

259

260 **Fluorescence Spectroscopy**

261 Dissolved organic matter (DOM) extracted from cryoconite sediment was analyzed using

262 excitation emission spectroscopy (EEMs). Scans were collected over an excitation range

263 of 240–450 nm in 10 nm increments and emission was monitored from 300–560 nm in 2

264 nm increments on a Fluoromax-4 spectrofluorometer (HORIBA Jobin-Yvon). Samples

265 were analyzed for UV absorbance with a Thermo Scientific Genesys 10 scanning UV

266 spectrophotometer from 190-1100 nm on optically dilute samples (absorbance values <

267 0.3 at 254 nm). EEMs data were post-processed to correct for instrument-specific bias

268 using manufacturer-generated correction files for excitation, emission, and blank

269 subtraction. Specific regions of fluorescence were defined for each carbon source

270 corresponding to previously identified natural organic matter fluorophores [24].

271 Fluorescence intensity values in the proteinaceous regions (B and T fluorophores) were

272 summed and classified as more-labile, while humic-like fluorescence regions (A and C

273 fluorophores) were combined and classified as less-labile and more recalcitrant. The

274 fluorescence for both defined regions was individually summed for the two samples

275 (cryoconite water and sediment extracted DOM).

276

277 **Sediment Analysis**

278 Powder X-ray diffraction (XRD) was used to determine the mineralogical composition of

279 studied cryoconite sediment. Samples were ground into a homogenous powder with a

280   mortar and pestle to homogenize the sediment mixture. XRD analysis was completed

281   with a Scintag XGen-4000 X-ray Powder Diffraction Spectrometer. X-ray spectra were

282   generated across a 2θ range of 5-70° in 0.02° steps with a scan rate of 2° min^{-1} for an

283   initial survey and across regions of prominent peaks at 24 0.5° min^{-1} for greater detail. X-

284   ray spectra were analyzed using the Scintag Diffraction Management System for NT

285   (DMSNT) computer software package to determine peak positions and relative intensities

286   and subsequently compared to the International Centre for Diffraction Data (ICDD)

287   powder diffraction file catalog for identification of crystalline minerals. Stepwise thermo-

288   gravimetric analysis was conducted to determine bulk organic matter content and

289   composition following methods from [25]. Briefly, 500 mg sub-samples of cryoconite

290   sediment (in triplicate for each combustion temperature) were weighed and placed into

291   crucibles and dried for three days at 38ºC. Individual samples were weighed to obtain

292   sample dry weight. Samples were placed in a muffle furnace at four different combustion

293   temperatures (105ºC, 200ºC, 350ºC, and 520ºC) for 4 hrs. After combustion samples

294   were placed into a desiccator to cool, once cool samples were weighed for the second

295   time. The difference in the dry weight and the weight post combustion for each sample

296   represents the percent organic matter lost at different temperatures of ignition. These

297   percent differences were used to calculate the total organic content and different lability

298   classifications which has been previously described by [25-27]. The following

299   differentiations were used: the loss of water (38-200°C), thermolabile (200-350°C), and

300   stable organic matter (350-520°C) [28].

301

302

303 **Chemical Analyses**

304 Samples run in triplicate for chlorophyll a (chl *a*) extraction and analysis were filtered in

305 the dark through 25 mm pre-combusted GF/F filters wrapped in aluminum foil and kept

306 at -20°C until. Chl *a* was extracted in a 1:1 solution of 90% and dimethyl sulfoxide for 12

307 hrs in the dark at -20°C. Extracted chl *a* was analyzed with a Turner 10-AU fluorometer.

308 Anion samples in triplicate were filtered through 0.4 μm 47 mm nucleopore filters,

309 deionized water was used as a filtration blank, and samples were analyzed on a Dionex

310 ICS-1100 ion chromatography system.

311

312 **Supplementary Results:**
313
314 Fluorescent DOM was detected in both the cryoconite water and in the sediment

315 extracted DOM. The fluorescent signature of the sediment extracted DOM has

316 fluorescence in the B and T regions, compared to the water where fluorescence was only

317 present in the T regions. Similarly between both samples fluorescence was not detected in

318 the humic-like regions, rather the fluorescent DOM present was predominately in the

319 more-labile, microbially derived regions. The sediment extracted DOM was comprised of

320 89.07% more-labile DOM and 10.92% less labile DOM, and the overlaying water

321 consisted of 93.57% more-labile and 6.42% less labile DOM.

322   Simulation of organic matter leakage from a cell with a relatively large leakage

323 rate (0.5 d^{-120}) under standard conditions showed that there was an inversely proportional

324 relationship between the concentration of exuded organic matter and the distance from

325 the filament surface. Within the phycosphere of a filamentous cell, with a 1.99 μm radius,

326 10% of the cell surface concentration was estimated to extend 1um away of the cell

327   surface, and at 2 μm from the cell surface only 5% of the initial concentration will extend

328   (Figure SI 3). We therefore conclude that >2 μm is a conservative delineation where

329   exuded organic matter concentrations are too diffuse and below the threshold for bacterial

330   chemosensory detection.

331   **Supplementary References**
332
333   1.   Telling, J. *et al.* Spring thaw ionic pulses boost nutrient availability and
334   microbial growth in entombed Antarctic Dry Valley cryoconite holes. *Front*
335   *Microbiol* **5,** 694–694 (2014).
336   2.   Fountain, A. G., Tranter, M., Nylen, T. H., Lewis, K. J. & Mueller, D. R.
337   Evolution of cryoconite holes and their contribution to meltwater runoff from
338   glaciers in the McMurdo Dry Valleys, Antarctica. *Journal of Glaciology* **50,**
339   35–45 (2004).
340   3.   Fountain, A. G., Nylen, T. H., Tranter, M. & Bagshaw, E. Temporal
341   variations in physical and chemical features of cryoconite holes on Canada
342   Glacier, McMurdo Dry Valleys, Antarctica. *J. Geophys. Res.* **113,** G01S92
343   (2008).
344   4.   Foreman, C. M., Sattler, B., Mikucki, J. A., Porazinska, D. L. & Priscu, J. C.
345   Metabolic activity and diversity of cryoconites in the Taylor Valley,
346   Antarctica. *J. Geophys. Res.* **112,** G04S32 (2007).
347   5.   Bagshaw, E. A., Tranter, M. & Wadham, J. L. High-resolution monitoring
348   reveals dissolved oxygen dynamics in an Antarctic cryoconite hole. *Hydrol.*
349   *Process.* **25,** 2868–2877 (2011).
350   6.   Bagshaw, E. A. *et al.* Biogeochemical evolution of cryoconite holes on
351   Canada Glacier, Taylor Valley, Antarctica. *J. Geophys. Res.* **112,** (2007).
352   7.   Bagshaw, E. A. *et al.* Do Cryoconite Holes have the Potential to be
353   Significant Sources of C, N, and P to Downstream Depauperate Ecosystems
354   of Taylor Valley, Antarctica? *Arctic, Antarctic, and Alpine Research* **45,**
355   440–454 (2013).
356   8.   Caporaso, J. G. *et al.* QIIME allows analysis of high-throughput community
357   sequencing data. *Nat Meth* **7,** 335–336 (2010).
358   9.   Haas, B. J. *et al.* Chimeric 16S rRNA sequence formation and detection in
359   Sanger and 454-pyrosequenced PCR amplicons. *Genome Res.* **21,** 494–504
360   (2011).
361   10.   Huber, T., Faulkner, G. & Hugenholtz, P. Bellerophon: a program to detect
362   chimeric sequences in multiple sequence alignments. *Bioinformatics* **20,**
363   2317–2319 (2004).
364   11.   Musat, N. *et al.* A single-cell view on the ecophysiology of anaerobic
365   phototrophic bacteria. *Proc. Natl. Acad. Sci. U.S.A.* **105,** 17861–17866
366   (2008).
367   12.   Manz, W., Amann, R., Ludwig, W., Vancanneyt, M. & Schleifer, K.-H.
368   Application of a suite of 16S rRNA-specific oligonucleotide probes designed
369   to investigate bacteria of the phylum cytophaga-flavobacter-bacteroides in
370   the natural environment. *Microbiology* **142**, 1097-1106 (1996).
371   13.   Foster, R. A. *et al.* Nitrogen fixation and transfer in open ocean diatom–
372   cyanobacterial symbioses. *ISME J* **5,** 1484–1493 (2011).
373   14.   Polerecky, L. *et al.* Look@NanoSIMS--a tool for the analysis of nanoSIMS
374   data in environmental microbiology. *Environ. Microbiol.* **14,** 1009–1023
375   (2012).
376   15.   Sun, J. Geometric models for calculating cell biovolume and surface area for

377   phytoplankton. *Journal of Plankton Research* **25,** 1331–1346 (2003).

378 16. Verity, P. G. *et al.* Relationships between cell volume and the carbon and
379   nitrogen content of marine photosynthetic nanoplankton. *Limnol. Oceanogr.*
380   **37,** 1434–1446 (1992).

381 17. Musat, N. *et al.* The effect of FISH and CARD-FISH on the isotopic
382   composition of ^{13}C- and ^{15}N-labeled Pseudomonas putida cells measured by
383   nanoSIMS. *Systematic and Applied Microbiology* 1–10 (2014).

384 18. Stocker, R. The 100 μm length scale in the microbial ocean. *Aquat Microb*
385   *Ecol* **76,** 189–194 (2015).

386 19. Bell, W. & Mitchell, R. Chemotactic and Growth Responses of Marine
387   Bacteria to Algal Extracellular Products. *Biological Bulletin* **143,** 265 (1972).

388 20. Jackson, G. A. Simulating chemosensory responses of marine
389   microorganisms. *Limnol. Oceanogr.* **32,** 1253–1266 (1987).

390 21. Mullin, M. M., Sloan, P. R. & Eppley, R. W. Relationship Between Carbon
391   Content, Cell Volume, and Area in Phytoplankton. *Limnol. Oceanogr.* **11,**
392   307–311 (1966).

393 22. R Development Core Team. R: a language and environment for statistical
394   computing. Vienna, Austria: R Foundation for Statistical Computing. (2012).

395 23. Chen, M.-Y., Lee, D.-J., Tay, J.-H. & Show, K.-Y. Staining of extracellular
396   polymeric substances and cells in bioaggregates. *Appl Microbiol Biotechnol*
397   **75,** 467–474 (2007).

398 24. Coble, P. G. Characterization of marine and terrestrial DOM in seawater
399   using excitation-emission matrix spectroscopy. **51,** 325–346 (1996).

400 25. Kristensen, E. Characterization of biogenic organic matter by stepwise
401   thermogravimetry (STG). *Biogeochemistry* **9,** 135–159 (1990).

402 26. Walter E Dean, Jr. Determination of Carbonate and Organic Matter in
403   Calcareous Sediments and Sedimentary Rocks by Loss on Ignition:
404   Comparison With Other Methods. *SEPM JSR* **Vol. 44,** 242–248 (1974).

405 27. Langford, H., Hodson, A., Banwart, S. & Bøggild, C. The microstructure and
406   biogeochemistry of Arctic cryoconite granules. *Annals of Glaciology* **51,** 87–
407   94 (2010).

408 28. Cuypers, C. *et al.* Amorphous and condensed organic matter domains: the
409   effect of persulfate oxidation on the composition of soil/sediment organic
410   matter. *Chemosphere* **48,** 919–931 (2002).

411

412

413   **Supplementary Figures:**
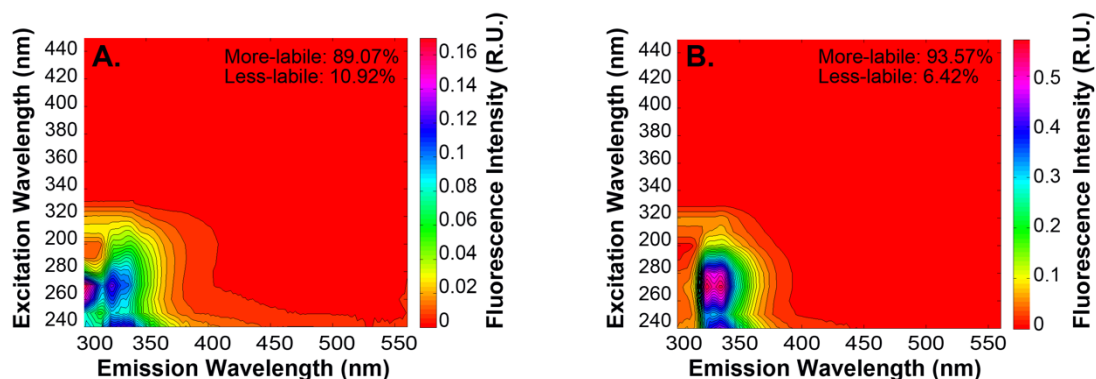
414
415   Figure S1: 3D EEM of cryoconite DOM extracted from sediment (A.) and cryoconite
416   water (B.) and corresponding percentages of more- and less-labile components.
417
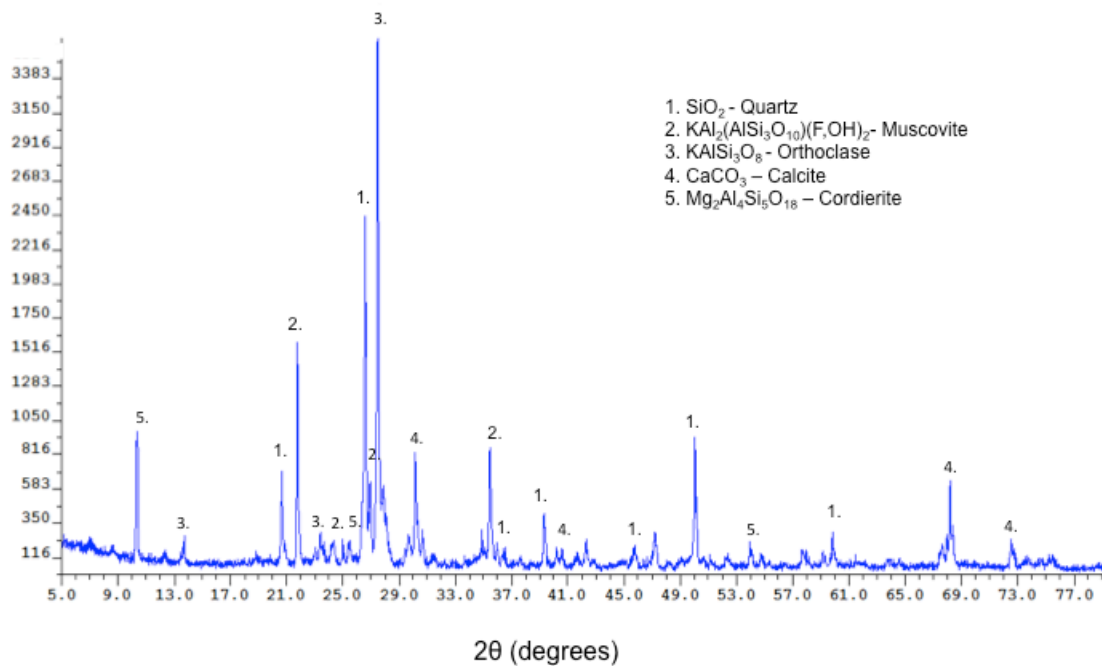
418
419   Figure S2: Powder XRD spectral profile of cryoconite sediments, used to illustrate the
420   interpretation of present constituents. Cryoconite sediment diffraction patterns suggest a
421   dominance of silicate materials, specifically quartz and corresponding weathering
422   products.
423

424
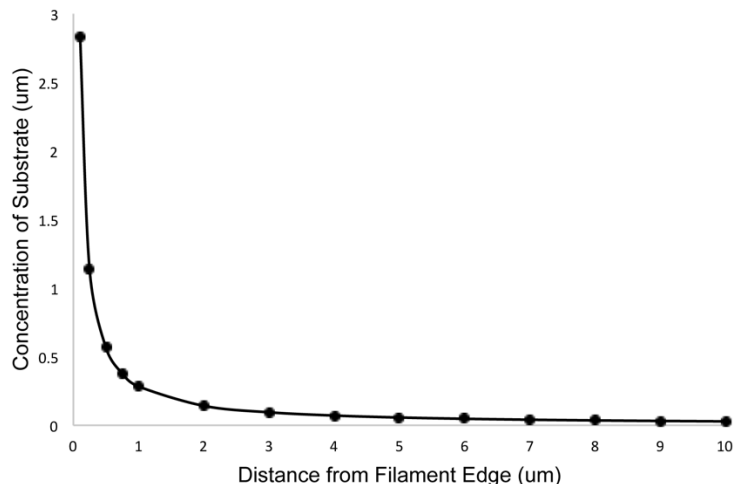
Figure S3: Concentration of exuded organic matter in the boundary layer of a cell with a
1.99 μm radius, assuming an exudation rate of 0.5 d^{-1} (Jackson 1987).

427

Supplementary Tables:

A. Bacterial Community		B. Cyanobacterial Community	
Phylum Level Taxonomic Classification	Relative Abundance (%)	Genus Level Taxonomic Classification	Relative Abundance (%)
Acidobacteria	0.94	*Tolypothrix*	8.61
Actinobacteria	23.69	*Chamaesiphon*	6.55
Bacteroidetes	18.81	*Pseudanabaena*	5.84
Chloroflexi	0.04	*Nostoc*	12.16
Cyanobacteria	27.37	*Phormidium*	4.56
Firmicutes	3.80	*Oscillatoria*	61.30
Gemmatimonadetes	1.93	Unclassified	0.98
Planctomycetes	1.46		
Proteobacteria	21.68		
Unclassified	0.29		

429

Table S1: Comparison of the relative abundances of 454 Pyrosequencing sequences for
A.) dominant cryoconite sediment organisms at the phylum taxonomic classification level
and B.) Cyanobacterial sequences at the genus classification.

433

Temperature	Sample Average % Dry Weight ± SD	Classification	Description
38-105°C	0.49 ± 0.73	Loss of Water	Crystalline lattice water, and hygroscopic water of salts and organic matter
105-200°C	4.3 ± 2.08		
200-350°C	2.19 ± 1.02	Thermolabile	Dominated by carbohydrates
350-520°C	0.76 ± 0.80	Stable Organic Matter	Oxidation of aromatic groups (lignin, humic substances, kerogens) and char

434

435 Table S2: Triplicate thermo-gravimetric analysis of organic matter (as percentage of dry
436 weight) from cryoconite sediments, and characterization of organic matter present
437 (Kristensen, 1990). Total organic matter accounted for 7.7% of the cryoconite dry weight.
438

OM (% of dry weight)	Cl^- (mg/L)	NO_2^- (mg/L)	NO_3^- (mg/L)	Br^- (mg/L)	PO_4^{-3} (mg/L)	SO_4^{-2} (mg/L)	Chl a ($\mu g\ L^{-1}$)	Bacteria (cells/g)
7.7	7.31	0.17	0.19	0.1956	0.1998	6.1846	0.22	1.86×10^{8} ($\pm 1.49 \times 10^{6}$)

439

440 Table S3: Biogeochemistry of cryoconite water and bacterial cell abundances plus or
441 minus the standard deviation (OM= organic matter, Chl a = chlorophyll a)
442

443

444

445

446
447
448
449